Kurdistan Journal of Applied Research (KJAR)
Print-ISSN: 2411-7684 | Electronic-ISSN: 2411-7706

Original Article

Check for updates

A Finite Element Study on the Structural Behavior of a Dual-Axis Solar Tracking System

Rayan Rahal [a], Mark Matta [b], Jihad Rishmany [a*]

[a] Department of Mechanical Engineering, Faculty of Engineering, University of Balamand, Lebanon.
[b] Faculty of Technology, Policy and Management, Delft University of Technology, Netherlands.

Submitted: 06 December 2025
Revised: 12 February 2026
Accepted: 20 February 2026

*** Corresponding Author**:
Jihad.rishmany@balamand.edu.lb

Keywords: Dual-axis solar tracker, Finite element analysis, Optimal tilt angle, Wind load, Structural integrity assessment.

How to cite this paper: R. Rahal, M. Matta, J. Rishmany," A Finite Element Study on the Structural Behavior of a Dual-Axis Solar Tracking System ", KJAR, vol. 11, no. 1, pp: 51-65, Jun 2026, doi: 10.24017/science.2026.1.4

Abstract: Solar panels have become a highly effective and widely adopted source of renewable energy. Extensive research has been devoted to improving the materials used in photovoltaic systems to enhance efficiency, durability, and performance. Continuous efforts have also focused on strategies to maximize solar energy capture; from materials used to determining the optimal angle and direction for panel installation for optimal energy capture. Within this context, this study presents the design and structural analysis of an innovative dual-axis solar tracker, developed and simulated using SolidWorks. The design consists of three main components: the main structure, which can hold up to a total of 18 panels arranged in a 3x6 matrix; the rotating structure, to which the main structure is attached via two flanged bearings at the ends to provide tilt motion; and the stationary base, to which the rotating structure is connected via a slew bearing that enables rotation in the east-west direction. The overall design accounts for a total system weight of approximately 4000 kg. To ensure safe operation, Finite Element Analysis is conducted under extreme-case wind loading conditions to assess structural integrity. Key results included a maximum von Mises stress of 196.6 MPa, a maximum deflection of 37.81 mm, and a minimum factor of safety of 1.122. Convergence is successfully achieved for all components, with relative errors below 1%, confirming the reliability and accuracy of the simulation outcomes.

1. Introduction

Solar energy has witnessed unprecedented global growth over the past decade; from 2013 to 2023, installed solar capacity increased by approximately 1,060%, rising from about 138 GW to nearly 1.6 TW [1]. Moreover, global solar installations added approximately 380 GW of new capacity in 2025, representing an increase of about 64% compared to the additions recorded during the same period in 2024 [2].

Current research focuses on increasing the efficiency of PVs, with a current all-time high of 30% and an expectation to reach 50% by 2030 [3].The energy produced by a solar panel is highly affected by its direction and angle of mounting [4]. To maximize energy production, the panel should face the sun's rays at a 90-degree angle; this requires a dual-axis tracking [5]. There are three main mounting methods for solar panels: fixed, single-axis, and dual-axis. The single-axis includes two types: seasonal monitoring or tracking the sun from west to east. The dual-axis system combines them both [6].

George and Anto [7] worked on three different computational methods to obtain the optimal tilt angle. They concluded that mounting the panels at the optimal angle daily could increase energy by up to 12%, and a change of 5 degrees from the optimal angle could cause a 2% decrease in performance. Mamun *et al*. [8] conducted a similar study, where they compared the power output with the tilt angle, resulting in a 3.54W decrease for every 5-degree change in the tilt angle.

The studies above highlighted the importance of the panel's direction relative to the sun. Sungur [9] experimented with two identical panels, where one of the panels was stationary and the other was mobile and tracking the sun's position. Plotting the power against time for each panel showed that the tracking system achieved 42.6% more energy than the fixed system. Chang *et al.* [10] conducted a similar study where they compared a fixed, single, and dual-axis system. The dual-axis system generated 17.46% more energy than the single-axis and 53.08% more than the fixed system. Mohanapriya *et al.* [11] concluded that a dual-axis tracker provides 40% more energy than a fixed system. Kuttybay *et al.* [12] discussed different control systems for solar trackers and how these systems provided an increase in energy varying from a minimum of 37.5% to a maximum of 52.7%.

It is important to mention that many dual-axis solar tracker designs already exist in the market, but most are proprietary to private companies and rarely published in detail. Trackers rely on complex mechanisms, such as power screws for tilt adjustment, which add more components, increasing both equipment and maintenance costs [13]. In addition, most designs are built close to the ground, leaving the space beneath them unusable, similar to conventional fixed solar panels [14].

To address these limitations, this work presents a dual-axis solar tracker that is intentionally elevated to provide sufficient ground clearance of 4.93 m. This exceeds the minimum clearance for highway bridges of 16 ft (4.87 m) [15], allowing safe vehicle passage in parking areas and agricultural fields. In addition, the proposed design offers improved tracking performance, reduced mechanical complexity, and enhanced economic feasibility. This elevation directly influences the structural configuration, load distribution, and overall stability, which are evaluated through finite element analysis to ensure adequate resistance to natural loads and reduced maintenance requirements.

The remainder of this article is organized as follows: Section 2 presents the materials and methods and includes all methodological components, namely the design requirements, wind-load definitions, preliminary design process, sizing strategy, material selection, and development of the Finite Element Model. Section 3 report results, including stress distribution, deflection behavior, factors of safety, and overall structural performance. Section 4 discuss the results and Finally, Section 5 concludes the study and provides a feasibility analysis and payback-period assessment to evaluate the economic viability of the proposed dual-axis tracking system.

2. Materials and Methods

To ensure a rigid and functional design, it is essential to understand and account for the system's operation and the external natural forces acting on it. To achieve this, critical factors such as operating angle, wind force, and material selection must be carefully considered.

2.1. Operating Angle

The site's latitude plays a role in determining the system's operating angle. The minimum and maximum angles are calculated based on the declination angles corresponding to the summer solstice (June 21st) and winter solstice (December 22nd) [16, 17].

The tilt angle can be calculated using Equation 1 [18].

$$\beta = |\phi - \delta| \qquad (1)$$

Where β is the tilt angle relative to the horizontal, ϕ is the latitude of the location, and δ is the declination angle. In this case, a latitude of 33° is used as a representative value.

The declination angle (δ) is given by equation 2.

$$\delta = 23.45 \sin\left(360 \frac{284+n}{365}\right) \qquad (2)$$

Where n is the day number of the year, for the summer solstice (June 21st), n = 172, and for the winter solstice (December 22nd), n = 356.

Substituting n in equation 2 yields a declination angle of 23.5° on June 21 and -23.44° on December 22. Using Equation 1 yields a minimum tilt angle of 9.5° on June 21 and a maximum tilt angle of 56.44° on December 22. Hence, the design operating angles will be between 5° and 60° to the horizontal.

2.2. Wind Load

After calculating the operating angle, the next step is to study the wind load design and tailor the design accordingly. In the United States, wind loads are established based on maps from the ASCE 7 standard, which is referenced by the International Building Code. These maps define basic wind speeds with a 50-year mean recurrence interval, expressed as 3-second gusts measured at 10 meters above ground in Exposure Category C. For example, under International Building Code 2009, which adopts ASCE 7-05, many regions using Exposure C are assigned a basic wind speed of approximately 100 mph (about 162 km/h). These values are then adjusted using exposure, importance, and topographic factors to determine the final design wind pressures [19, 20].

Under the older Uniform Building Code (UBC 1997), wind speeds were defined using the fastest-mile wind speed, with design values ranging from 80 to 110 mph (approximately 129 to 177 km/h) depending on exposure and region [21].

Hence, a wind speed of 162 km/h is used in this study, as it appropriately reflects a high-exposure condition relevant to the design scenario. This wind speed will be used to calculate the wind pressure at a 60-degree angle relative to the horizontal, which represents the most critical angle for incoming winds. The calculation is based on Chapter 29 of the building code ASCE 7-16, which states that any panel angled greater than 45 degrees can be considered a solid sign, and from which equation 3 is used to calculate the wind pressure [22].

$$p = q_h G C_f \qquad (3)$$

Where:
G: Gust effect Factor
C_f: Net force coefficient
q_h: Velocity pressure evaluated at height h, in psf, given by equation 4

$$q_h = 0.00256 G\ K_z\ K_{zt} K_d K_e V^2 \qquad (4)$$

K_z: velocity pressure exposure coefficient
K_{zt}: Topographic factor
K_d: Wind directionality factor
K_e: Ground elevation factor
V: Basic wind speed, in mph

$$q_h = 0.00256 G\ K_z\ K_{zt} K_d K_e V^2 \qquad (5)$$

To determine the coefficient values, Exposure B was selected based on the site conditions, from which the wind exposure coefficients Kz = 0.7187 and Kzt = 1.0 were obtained. The directionality factor Kd = 0.85 was taken in accordance with table 26.6-1 of ASCE 7-16, while an elevation factor Kc = 1.0 was assumed for sea-level conditions. As stated previously; to consider a conservative scenario, Exposure C was adopted for the wind speed of 162 km/h (101 mph) was used for V.

Substituting the values yields a velocity pressure (q_h) of 18.622 psf and a pressure (p) of 26.727 psf.

Projecting the wind pressure onto the normal axis of the panels seen in equation 5:

$$p_n = 26.727 \times \sin(60) = 23.146\ psf \qquad (5)$$

This is equivalent to 1.110 kPa.

2.3. Materials

The main objective of the dual-axis solar tracker is to maintain a feasible and practical design, which requires selecting materials that are available and cost-effective. Market research indicates that commonly accessible structural steel grades in many regions include S235JR, S275JR, and S355JR, all of which conform to the European standard EN 10025-2. According to Eurocode EN 1993-1-1, these grades have nominal yield strengths of 235 MPa, 275 MPa, and 355 MPa, respectively [23].

Based on considerations of availability, performance, and cost, S235JR is selected as the structural material for this study, as it offers a suitable balance between mechanical properties and economic viability, supporting the overall feasibility of the system.

2.4. Preliminary Design

The goal of the preliminary design is to achieve a system that allows the solar panels to remain perpendicular to the sun's rays throughout the day and across the year. To accomplish this, one component must rotate independently to follow the sun's elevation, while another part rotates with the sun's azimuthal movement throughout the day.

As illustrated in figure 1, the dual-axis solar tracker consists of three primary components: the main structure that supports 18 solar panels arranged in a 3×6 matrix; a rotating structure, connected to the main frame via two flanged bearings. This enables tilt to optimize the panels' orientation relative to the sun's elevation. This rotation ranges from 0 to 360 degrees and is driven by a motorized slew bearing and a stationary base that supports the entire, allowing rotation in the east-west direction and providing full 360-degree azimuthal rotation.

This dual-axis tracking capability enables continuous adjustment of both azimuth and elevation angles, significantly enhancing solar exposure and energy capture.

2.5. Sizing and Material Selection

A static analysis is conducted considering various loading conditions, including the system's weight and external forces such as wind load to assess stress distribution, deflection, and safety margins under extreme-case operational scenarios.

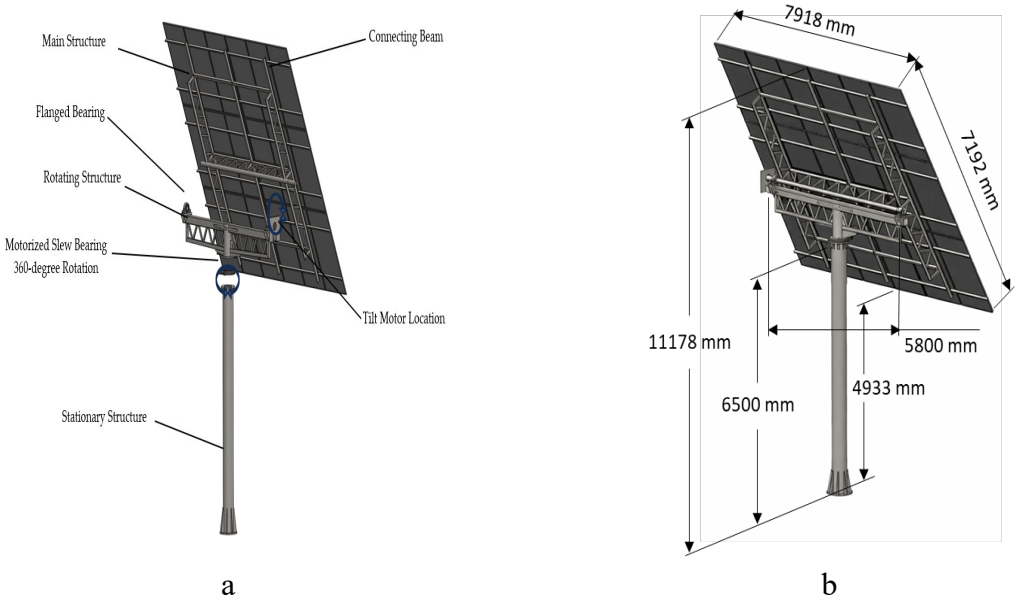

Figure 1: CAD drawing of the solar tracker system, (a) Exploded view, (b) Structure dimensions in millimeters.

2.6. *Finite Element Model*

The main structure is designed using structural members such as square, circular, and rectangular tubes. Gussets are strategically added to reinforce welded corners and improve load transfer at critical joints. In the Finite Element model, the structural frame is represented using beam elements (figure 2-a), while the solar panels are modeled as 2D surface bodies (figure 2-b) to capture their stiffness and distributed loading. Similarly, the gussets are also modeled as 2D elements to realistically represent their contribution to joint rigidity. A finite element mesh is then applied to both the frame and the panels to enable accurate numerical analysis.

Mesh size plays a crucial role: the finer the mesh, the higher the computational accuracy; however, this comes at the cost of increased computational time. Since every simulation is different, there's no rule for finding the best mesh quality; it often depends on the specific case [24].

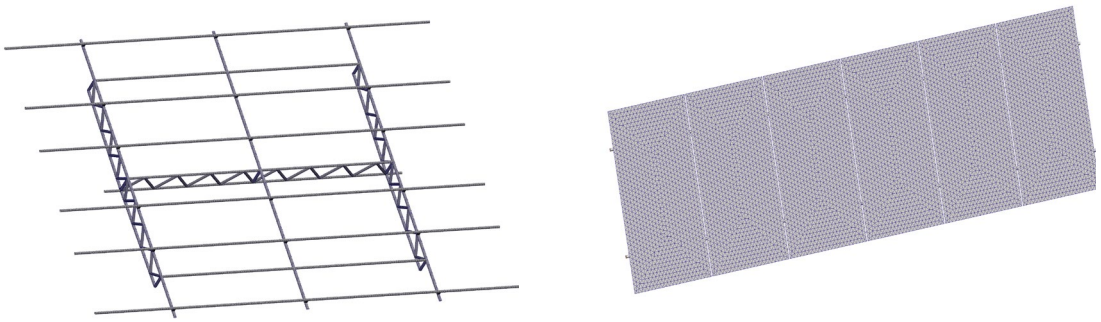

a b

Figure 2: Finite element model, (a) Meshing of the main frame, (b) Meshing of panels.

To ensure accuracy, mesh should be refined gradually until the results converge [25]. Figure 3 illustrates the convergence of the main structure, showing the maximum von Mises stress and displacement on the y-axis plotted against the number of degrees of freedom (DOF) on the x-axis. A finer mesh corresponds to a higher number of DOF. The values in figure 3 converge to a relative error of 0.613%. According to different articles, convergence is considered achieved when the percentage difference between two successive values, either in maximum von Mises stress or displacement, falls below 7% [26].

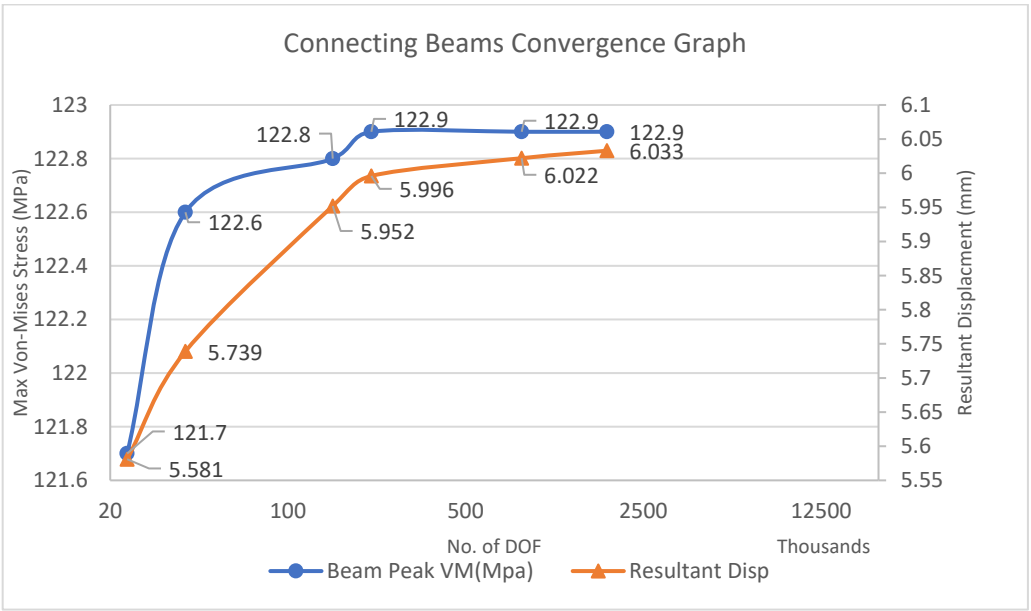

Figure 3: Maximum von-mises stresses and displacement against degree of freedom.

2.7. *Finite Element Analysis*

The main frame is divided into four parts and consists of three rows, each comprising six panels mounted on two connecting beams. Each beam is welded to the main structure at three locations, where fixed boundary conditions are applied at the corresponding nodes (pink nodes) in figure 4. The panel geometry and mass were defined using the specifications of Jinko Solar panels (model 66HL5-BDV). The panels are tilted at an angle of 60°, with the wind load applied perpendicular to the panel surfaces (red arrows), in addition to a gravity load acting downward (blue arrow). Static analysis yields an average reaction force at each fixed node of 2.270 kN in the y-direction and 2.990 kN in the z-direction, as summarized in table 1. The axis convention used is defined as the y-direction being vertical and the z-direction horizontal.

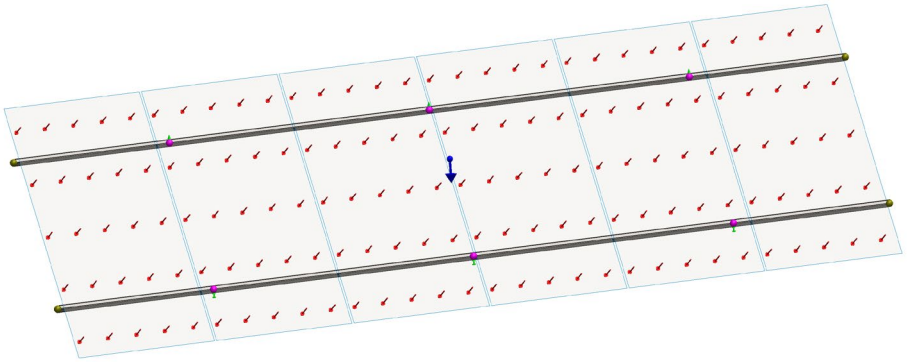

Figure 4: Boundary conditions and forces acting on the panel of the connecting beams.

Table 1: List of reaction forces for the connecting beams obtained from SolidWorks. These forces are the sum of all six nodes.

Component	Reaction Force (N)
Sum X:	0.00085449
Sum Y:	13517
Sum Z:	17937
Resultant:	22479

In addition to verifying convergence, the total external forces and system weight are manually computed and compared with the reaction forces obtained from the simulation.

- Mass per panel = 40 Kg
- Area per panel = 3.11 m²
- Wind pressure per panel = 1110 Pa
- Mass of two connecting beams (Obtained from SolidWorks) = 82.2 Kg
- Weight of System = (Weight Of Pannels x No. of pannels + Mass of Connecting Beam)x Gravity
$$= (40 \times 6 + 82.2) \times 9.81$$
$$= 3161 \text{ N}$$
- Force due to wind load = Area per panel x Wind Pressurex No. of Pannels
$$= 3.11 \times 1110 \times 6$$
$$= 20713 \text{ N}$$
- Vertical Force Component due to wind = $20713 \times \cos(60) = 10356.5$ N
- Horizontal Force Component Due to Wind = $20713 \times \sin(60) = 17937$ N
- Calculated Total Vertical Force = Vertical Force Component due to wind + Weight of the system
$$= 10356.5 + 3161$$
$$= 13517.5 \text{ N}$$

13517.5 N is the Sum of Vertical Forces from one row of panels.

17937 N is the Sum of Horizontal Forces acting on one row.

By comparing the results, it is observed that the applied loads are in accordance with the reaction forces obtained from SolidWorks in table 1.

Next, the reaction forces obtained from the connecting beams are applied to the main structure at 18 nodes, which represent the total number of contact points between the connecting beams and the main structure (figure 5-a). The forces in the y-direction are indicated by orange arrows, while those in the z-direction are represented by cyan arrows. The blue arrow denotes gravity, and the green arrows indicate the fixed nodes.

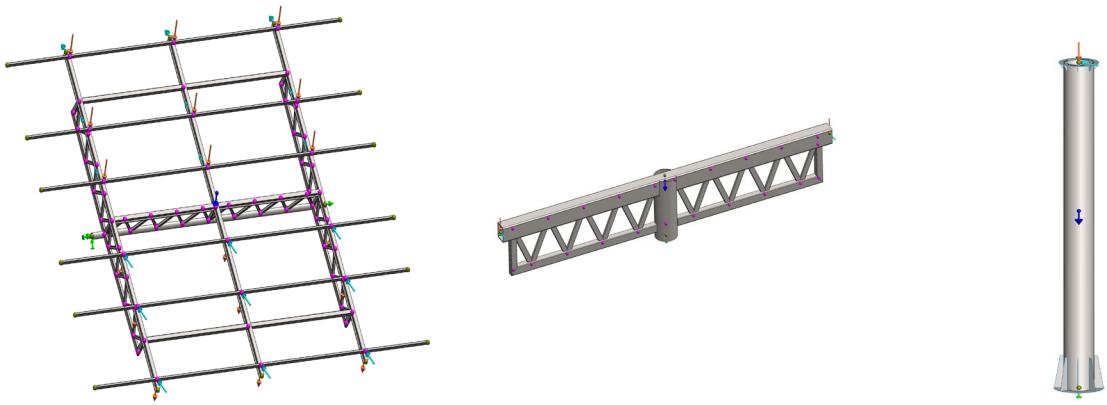

a b c

Figure 5: Boundary conditions and forces, (a) applied on main structure, (b) transferred from the main structure onto the rotating structure, (c) applied by the external loads and the weight of the entire system onto the stationary structure.

The average reaction force obtained from the main structure at each node is 50.80 kN in the y-direction (orange arrows) and 53.82 kN in the z-direction (cyan arrows) (Table 2). These forces are then translated to the rotating structure at two nodes (figure 5-b), where the flanged bearings are fixed.

Table 2: List of reaction forces for the main structure obtained from SolidWorks. These forces are the sum of all six nodes.

Component	Reaction Force (N)
Sum X:	0
Sum Y:	50802
Sum Z:	53820
Resultant:	76836

Finally, the reaction forces obtained from the rotating structure are 56.489 kN in the y-direction and 53.820 kN in the z direction (Table 3). These forces are translated from the rotating structure through the slew bearing onto the stationary structure. All boundary conditions and forces are represented in figure 5-c.

Table 3: List of reaction forces for the rotating structure obtained from SolidWorks. These forces are the sum of all six nodes.

Component	Reaction Force (N)
Sum X:	0
Sum Y:	56489
Sum Z:	53820
Resultant:	78023

Table 4: List of reaction forces for the stationary structure obtained from SolidWorks. These forces are the sum of all six nodes

Component	Reaction Force (N)
Sum X:	0
Sum Y:	67432
Sum Z:	53812
Resultant:	86295

Applied loads on the stationary structure:

- Sum of Vertical Force from one row of panels (Calculated previously) = 13517.5 N
- Mass of Main, rotating, and stationary structure (Obtained from SolidWorks) = 2740 Kg
- Sum of vertical Forces:

$$= \text{Mass of Main, rotating, \& stationary structure x Gravity} + \text{No. Of Rows x Sum of Vertical Force}$$
$$= (2740 \times 9.81) + (3 \times 13517.5)$$
$$= 67431.9 \text{ N}$$

- Sum of Horizontal forces $= \text{Sum of Horizontal Forces on one row x No. of rows}$

$$= 17937 \times 3$$
$$= 53811 \text{ N}$$

The Calculated Sum of Forces in the Horizontal and vertical direction at the bottom node of the stationary structure align with the reaction forces obtained from solid works in table 4. The reaction forces acting on the fixed nodes at the bottom of the stationary structure will be essential for the future design of the system's foundation. However, this study does not cover foundation design, as the primary focus is on evaluating the structural integrity of the steel frame. This section outlined the simulation methodology and explained how the forces were applied to each part of the structure. Next, the obtained results are evaluated and discussed.

3. Results

3.1. Stress Results

This chapter presents the stresses acting on each component of the structure. Figure 6-a illustrates the stress distribution in the connecting beams resulting from the wind load acting on the panels, which transfers forces to the connecting beams. As expected, the maximum stress of 122.8 MPa occurs in the region of the fixed end of the connecting beam, while the minimum stress is 0.546 MPa. For clarity, the fixed points are not visible in this figure; however, referring back to figure 3, it can be seen that the location of maximum stress corresponds to the fixed nodes (indicated by pink nodes). The stress distribution is consistent with the applied boundary conditions and loading scenario, and the maximum stress remains within the allowable stress range of the selected material, indicating a safe structural response under the applied loads.

For the main structure, figure 6-b shows a maximum stress of 196 MPa and a minimum stress of 138 MPa. The maximum stress represents the governing condition in this analysis and is therefore considered critical; its implications will be further assessed in the Factor of Safety section. It should be noted that this elevated stress is confined to a highly localized region of the structure. As stated earlier in the final design, stiffening ribs are added in these areas to enhance local stiffness and reduce stress concentrations. These ribs were not included in the present simulation due to the increased model complexity; additionally, the introduction of rigid elements in combination with beam elements led to non-physical stress concentrations and illogical results in SolidWorks, particularly in the vicinity of the rib regions. Consequently, the current analysis may be considered conservative.

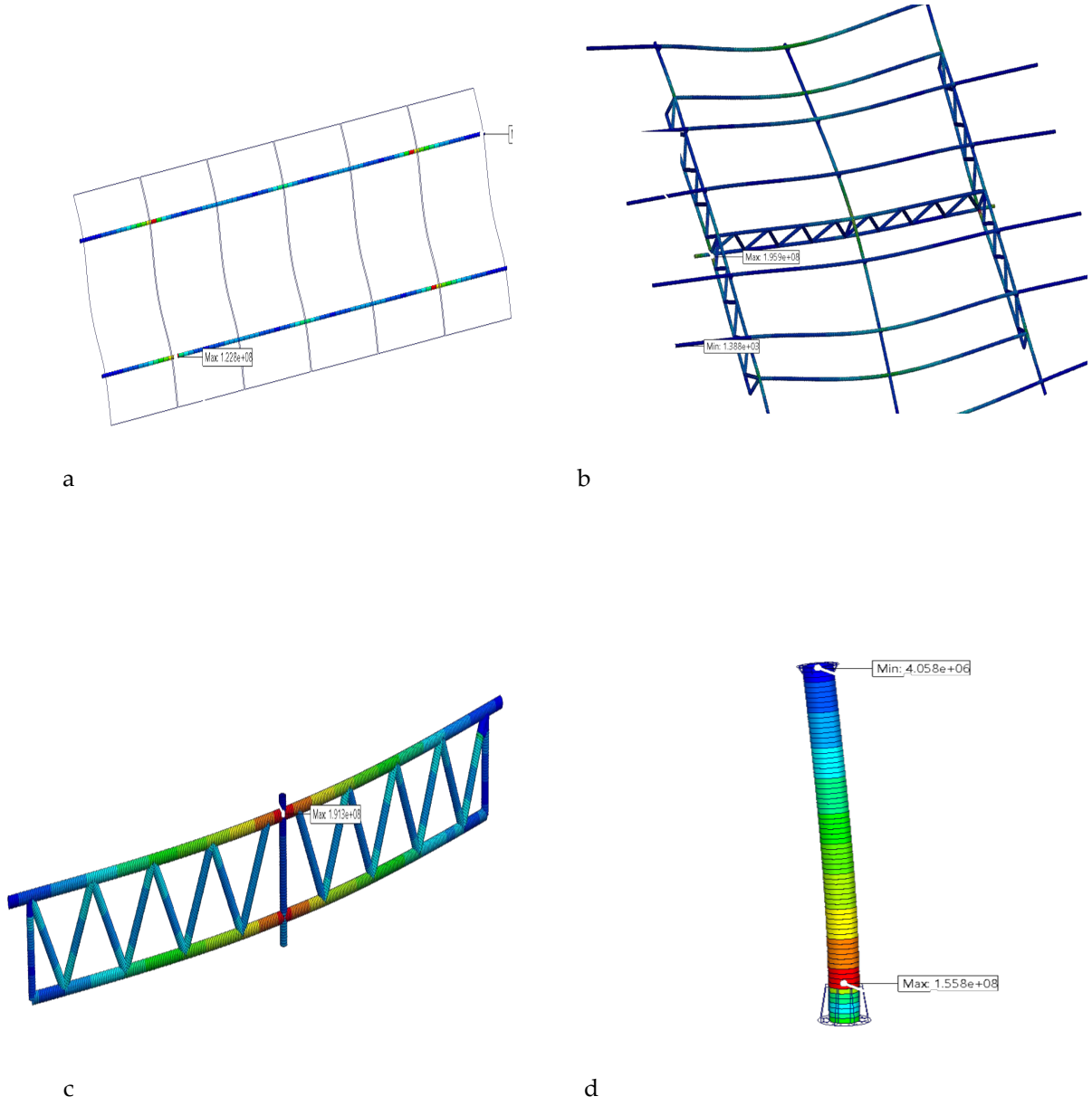

a b

c d

Figure 6: Von Mises plot for, (a) connecting beams, (b) main structure, (c) rotating structure, (d) stationary structure.

Similar to the main structure, the rotating structure shown in figure 6-c exhibits a critical maximum stress of 191.3 MPa. This stress is also highly localized, and additional stiffening ribs will be added to provide enhanced support and reduce local stress concentrations.

Finally, for the stationary structure in figure 6-d, a maximum stress of 155.8 MPa and a minimum stress of 4.058 MPa are observed, both of which fall within the acceptable stress limits of the selected material.

3.2. Displacement Results

Figure 7 illustrate the deformation profiles of each component. The stationary structure (figure 7-a) exhibits the maximum displacement of 37.81 mm, as it supports both the transmitted loading and the cumulative weight of upper components. Other parts (figure 7 b-c and d) show significantly lower displacements, indicating that the deformation is localized primarily at the base.

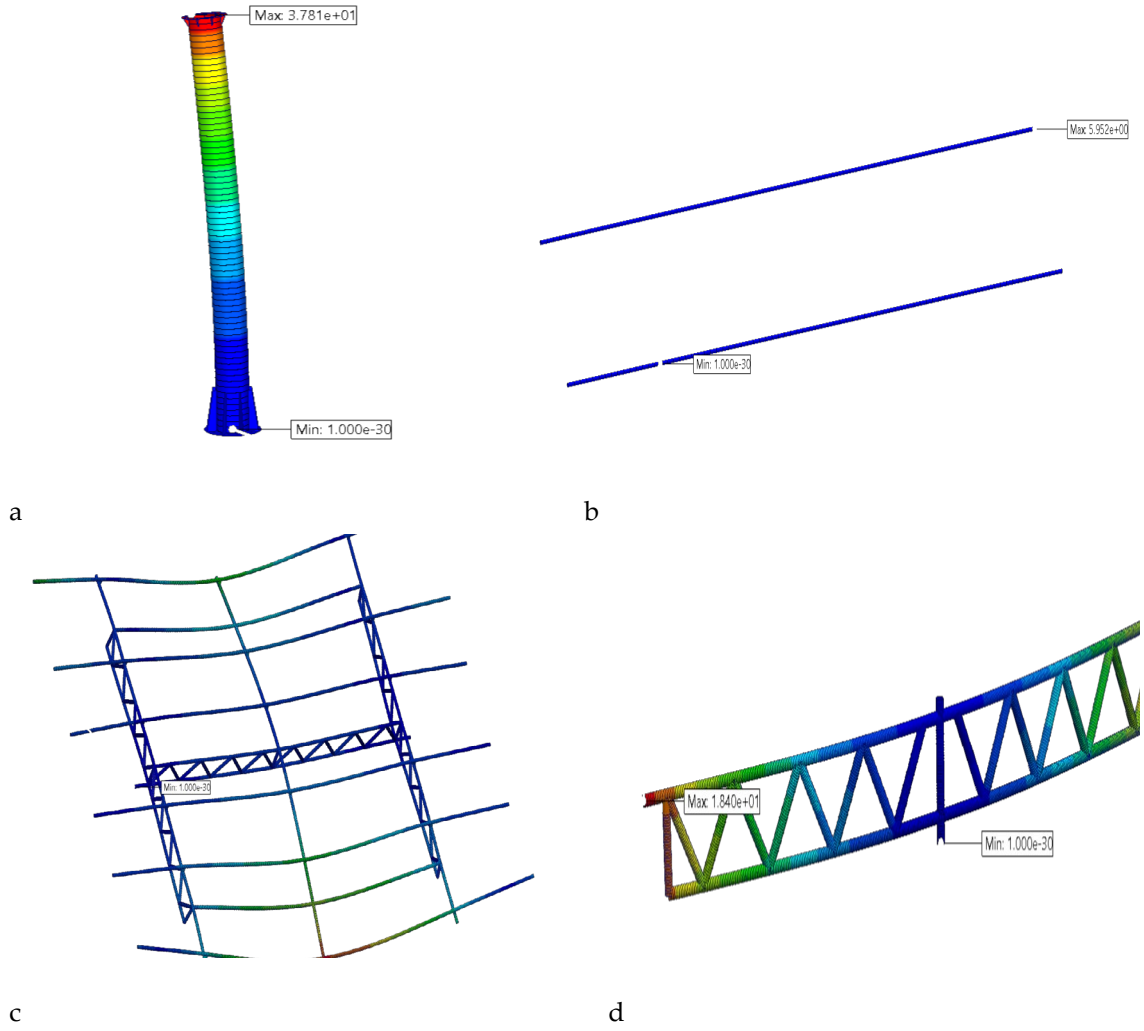

Figure 7: Displacement plot for, a) connecting beams, b) main structure, c) rotating structure, d) stationary structure

3.3. Factor of Safety

The factor of safety results, shown in figure 8, indicate a minimum value of 1.122 for the main structure. Although this value lies slightly above the critical limit of 1.0 and below common design recommendations (1.5–3.0), the simulation was conducted using a worst-case wind speed of 162 km/h, representing the upper limit defined by building codes for the region. As stated earlier, stiffening ribs will be added to reinforce the structure in high-stress regions, which is expected to increase the overall factor of safety.

In addition, the tracker also incorporates a dynamic safety mode, where panels automatically rotate to a 0° tilt angle (parallel to the ground) during extreme wind conditions, thereby significantly reducing the effective wind load acting on the structure.

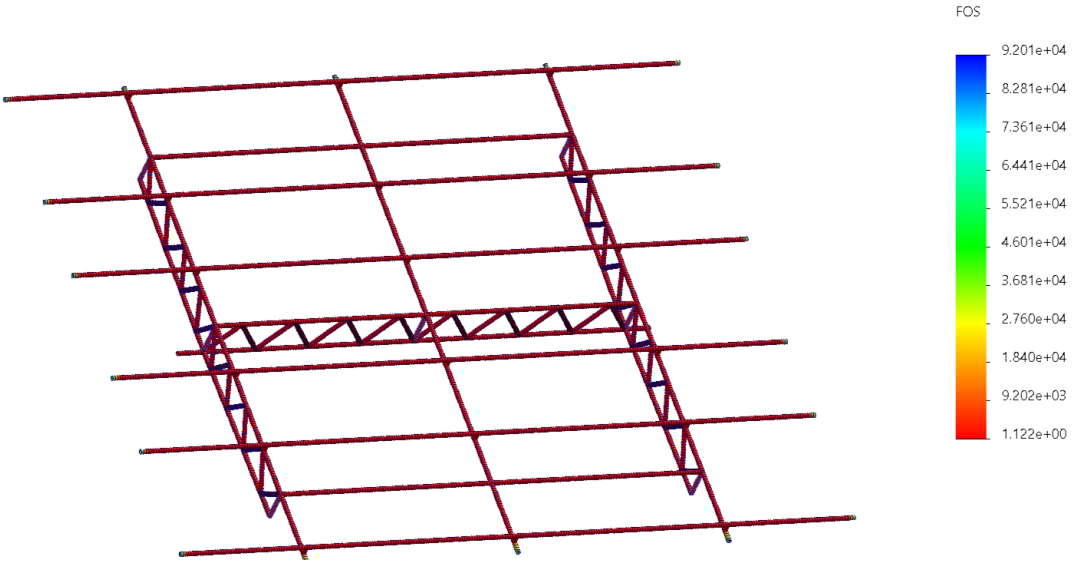

Figure 8: Main structure factor of safety plot.

3.4. Convergence Results

Convergence graphs for the main, rotating, and stationary structures (figures 9, 10 and 11) demonstrate stable stress and displacement values as the number of degrees of freedom increases. Relative error values across successive mesh refinements are below 1%, significantly lower than the acceptable 7% threshold. This confirms the reliability and numerical stability of the FEA results.

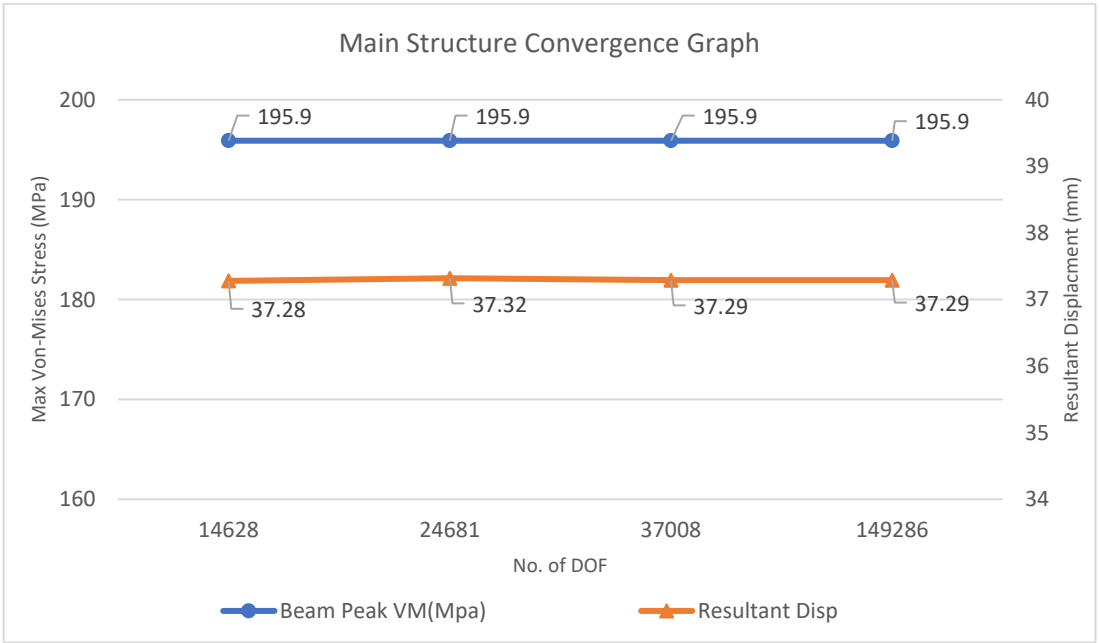

Figure 9: Maximum von-Mises stresses and displacement against DOF for the main structure.

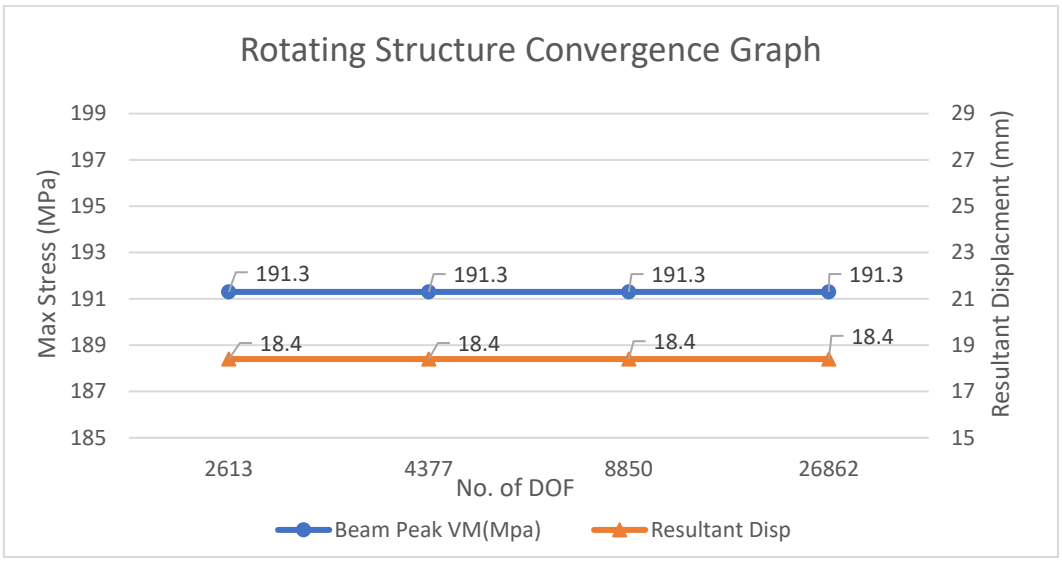

Figure 10: Maximum von-Mises stresses and displacement against degree of freedom for the rotating structure.

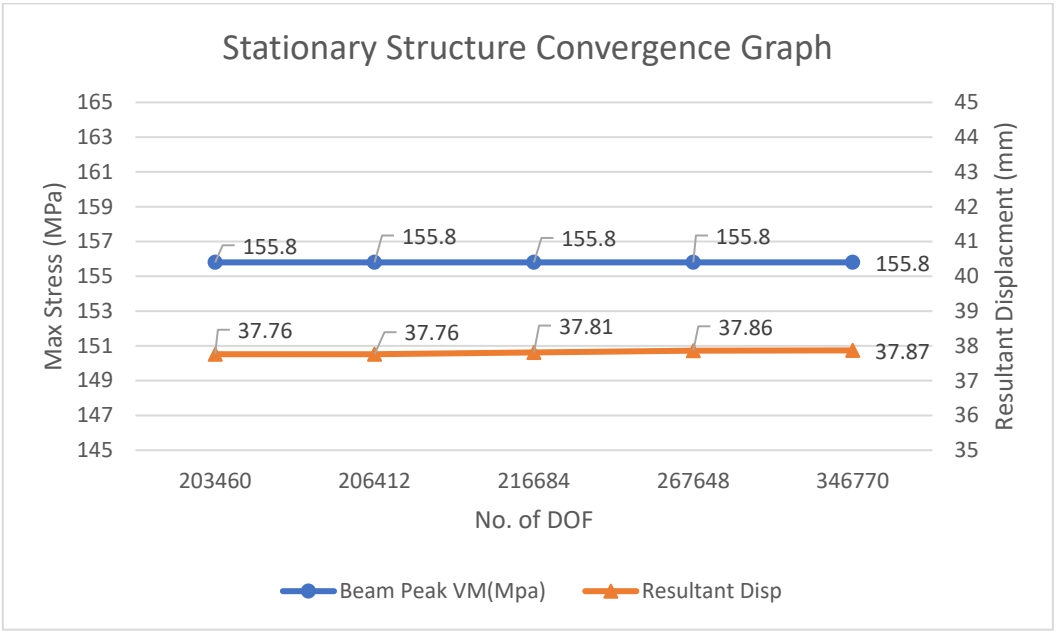

Figure 11: Maximum von-Mises stresses and displacement against degree of freedom for the stationary structure.

4. Discussion

The structural performance demonstrated in this study aligns with, and in several key areas improves upon, existing research on dual-axis solar tracking systems. Prior research by Ferroudji *et al.* [13] and Khelifi and Ferroudji [14] established that wind loading is the primary governing factor in tracker design, typically resulting in high stress concentrations at mechanical joints and support pillars. The current study confirms this pattern, with localized peak stresses of 196.6 MPa and 191.3 MPa occurring at critical connection points in the main and rotating structures, respectively. However, other studies evaluate trackers under standard conditions, this analysis utilized a conservative wind speed of 162 km/h (Exposure Category C), representing the upper limit for high-exposure regions. Despite these extreme loads, the system maintained a factor of safety of 1.122, which, while lower than general design standards of 1.5–3.0, is justified by the "worst-case" nature of the simulation and the planned addition of stiffening ribs in the final physical construction.

A significant differentiator of this design is its 4.93 m ground clearance. The literature, such as work by Khelifi and Ferroudji [14], notes that most commercial trackers are built close to the ground,

which restricts land use to solar energy production only. By exceeding the AASHTO [15] highway bridge requirement of 4.87 m (16 ft), the proposed design enables dual-use applications, such as agricultural harvesting or vehicle parking, without compromising structural stability.

This study provides a higher level of numerical transparency than many previous works. While some academic literature, such as Pisarciuc *et al.* [26], accepts a 7% relative error as a threshold for mesh convergence, this study achieved a relative error of below 1% (specifically 0.613% for the main structure). This rigorous convergence testing ensures that the reported stress and displacement values are stable and not artifacts of mesh density.

The decision to utilize a dual-axis system is supported by the findings of Sungur {9] and Chang *et al.* [10], who reported energy yield increases of 42.6% to 53.08% over fixed systems. Furthermore, the sensitivity of the system to its 5° to 60° seasonal tilt range is critical; as noted by George and Anto [7], even a 5-degree deviation from the optimal angle can result in a 2% performance loss. The current structural design successfully supports a 3x6 panel matrix necessary to capture these yield benefits while surviving extreme weather.

Consistent with the findings of Ferroudji *et al.* [13], the current analysis is limited to static loading. The study does not yet account for dynamic wind effects (vortex shedding) or fatigue behavior over a 20-year lifespan. Future research will incorporate these dynamic factors and optimize the weight of the S235JR structural steel frame to further improve economic feasibility.

Table 5 highlights the key parameters and methodological advancements of the proposed dual-axis solar tracking system versus existing designs.

Table 5: Comparison of current study vs. previous literature.

Parameter / Investigation	Findings in previous literature	Findings in this study (current work)
Ground clearance	Systems are typically built close to the ground, making the land beneath them unusable.	Elevated design (4.93 m), exceeding AASHTO highway bridge requirements (4.87 m) to allow for vehicle and machinery passage.
Wind load scenario	Wind loading is recognized as the governing factor, often causing stress at joints.	Simulated under a conservative "worst-case" wind speed of 162 km/h (Exposure Category C).
Numerical reliability	Many studies do not explicitly demonstrate mesh convergence.	Achieved rigorous mesh convergence with < 1% relative error, far exceeding the standard 7% threshold.
Maximum stress	Stress localization near joints and supports is common.	196.6 MPa (localized); confirmed to be within the yield strength of the selected material.
Safety features	Often proprietary or not detailed in structural literature.	Includes a dynamic safety mode where panels rotate to 0° tilt to reduce effective wind load during extreme events.
Energy efficiency	Dual-axis systems reported to increase energy by 37.5% to 53.08% over fixed systems.	Designed to support a 3x6 panel matrix (18 panels) to maximize energy capture as evidenced by cited efficiency gains.
Material choice	Often proprietary.	Utilizes S235JR structural steel for a balance of mechanical performance and economic viability.
Methodological Depth	Often limited to static loading.	Focused on static loading with manual verification of simulation reaction forces against calculated weights to ensure accuracy.

5. Conclusions

This study aimed to design and structurally evaluate an elevated dual-axis solar tracking system subjected to extreme wind loading conditions. A finite element model was developed in SolidWorks to assess the structural response of the system under a conservative wind speed of 162 km/h and gravitational loading.

The analysis results showed a maximum von Mises stress of 196.6 MPa, a maximum displacement of 37.81 mm, and a minimum factor of safety of 1.122. All stress values remained below the yield strength of the selected structural steel (S235JR). Mesh convergence was achieved for all structural components, with relative errors in stress and displacement below 1%, confirming the numerical accuracy and stability of the simulations. These results confirm that the proposed dual-axis solar tracker meets the structural performance objectives defined in this study.

Future work may focus on scaling the design to accommodate additional photovoltaic panels, optimizing member dimensions to reduce structural weight, and investigating alternative materials to improve strength-to-weight efficiency. Further numerical and experimental studies incorporating dynamic wind effects, fatigue behavior, and long-term service conditions may also be considered to extend the applicability of the proposed design.

Author contributions: Rayan Rahal: Conceptualization, Formal Analysis, Investigation, Software, Writing – original draft. **Mark Matta:** Conceptualization, Formal Analysis, Investigation, Software, Writing – original draft. **Jihad Rishmany:** Data curation, Methodology, Project administration, Resources, Validation, Writing – review & editing.

Data availability: Data will be available upon reasonable request by the authors.

Conflicts of interest: The authors declare that they have no known competing financial interests or personal relationships that could have appeared to influence the work reported in this paper.

Funding: The authors did not receive support from any organization for the conducting of the study.

References

[1] V. Vitaliy, "Solar energy growth in past 10 years in different countries," *SolarEnergies.ca*, Nov. 2024. Available: https://solarenergies.ca/solar-energy-growth-in-past-10-years/.

[2] Ember Energy, "Global solar installations surge 64% in first half of 2025," *Ember Energy*, Nov. 2025. [Online]. Available: https://ember-energy.org/latest-updates/global-solar-installations-surge-64-in-first-half-of-2025/. [Accessed: 22-Nov-2025].

[3] A. Garrod and A. Ghosh, "A review of bifacial solar photovoltaic applications," *Frontiers in Energy*, vol. 17, no. 6, pp. 704–726, Dec. 2023, doi: 10.1007/s11708-023-0903-7.

[4] R. Parthiban and P. Ponnambalam, "An enhancement of the solar panel efficiency: A comprehensive review," *Frontiers in Energy Research*, vol. 10, p. 937155, Jul. 2022, doi: 10.3389/fenrg.2022.937155.

[5] G. Li, R. Tang, and H. Zhong, "Optical performance of horizontal single-axis tracked solar panels," *Energy Procedia*, vol. 16, pp. 1744–1752, 2012, doi: 10.1016/j.egypro.2012.01.270.

[6] N. AL-Rousan, N. A. M. Isa, and M. K. M. Desa, "Advances in solar photovoltaic tracking systems: A review," *Renewable and Sustainable Energy Reviews*, vol. 82, pp. 2548–2569, Feb. 2018, doi: 10.1016/j.rser.2017.09.077.

[7] A. George and R. Anto, "Analytical and experimental analysis of optimal tilt angle of solar photovoltaic systems," in *2012 International Conference on Green Technologies (ICGT)*, IEEE, Dec. 2012, pp. 234–239. doi: 10.1109/ICGT.2012.6477978.

[8] M. A. A. Mamun, M. M. Islam, M. Hasanuzzaman, and J. Selvaraj, "Effect of tilt angle on the performance and electrical parameters of a PV module: Comparative indoor and outdoor experimental investigation," *Energy and Built Environment*, vol. 3, no. 3, pp. 278–290, Jul. 2022, doi: 10.1016/j.enbenv.2021.02.001.

[9] C. Sungur, "Multi-axes sun-tracking system with PLC control for photovoltaic panels in Turkey," *Renew Energy*, vol. 34, no. 4, pp. 1119–1125, Apr. 2009, doi: 10.1016/j.renene.2008.06.020.

[10] K.-C. Chang, Y. Zhou, H. Ullah, K.-C. Chu, T. Sajid, and Y.-C. Lin, "Study of low cost and high efficiency intelligent dual-axis solar panel system," in *2020 IEEE International Conference on Artificial Intelligence and Computer Applications (ICAICA)*, Dalian, China: IEEE, Jun. 2020, pp. 336–341. doi: 10.1109/ICAICA50127.2020.9182474.

[11] V. Mohanapriya, V. Manimegalai, V. Praveenkumar, and P. Sakthivel, "Implementation of dual axis solar tracking system," *IOP Conference Series Materials Science and Engineering*, vol. 1084, no. 1, p. 012073, Mar. 2021, doi: 10.1088/1757-899x/1084/1/012073.

[12] N. Kuttybay *et al.*, "Assessment of solar tracking systems: A comprehensive review," *Sustainable Energy Technologies and Assessments*, vol. 68, p. 103879, Aug. 2024, doi: 10.1016/j.seta.2024.103879.

[13] F. Ferroudji, T. Ouattas, and C. Khélifi, "Design, modeling and finite element static analysis of a new two axis solar tracker using SolidWorks/COSMOSWorks," *Applied Mechanics and Materials*, vol. 446-447, pp. 738–743, 2014 doi: 10.4028/www.scientific.net/AMM.446-447.738.

[14] C. Khelifi and F. Ferroudji, "Stress and fatigue analyses under wind loading of the dual axis sun tracking system via finite element analysis," *Journal of Mechanical Engineering and Sciences*, vol. 10, no. 2, pp. 2008–2015, 2016, doi: 10.15282/jmes.10.2.2016.5.0189.

[15] AASHTO LRFD Bridge design specifications, 10th ed., LRFDBDS-10, AASHTO, Washington, DC, USA, 2024. ISBN: 978-1-56051-828-0.

[16] N. Al-Messabi, C. Goh, and Y. Li, "Heuristic grey-box modelling for photovoltaic power systems," *Systems Science and Control Engineering*, vol. 4, no. 1, pp. 235–246, Jan. 2016, doi: 10.1080/21642583.2016.1228485.

[17] J. Page, "The role of solar-radiation climatology in the design of photovoltaic systems," in *McEvoy's Handbook of Photovoltaics: Fundamentals and Applications*, Elsevier Inc., 2018, pp. 601–670. doi: 10.1016/B978-0-12-809921-6.00016-1.

[18] M.A. Danandeh, S.M. Mousavi G., "Solar irradiance estimation models and optimum tilt angle approaches: A comparative study," *Renewable and Sustainable Energy Reviews*, Volume 92, Pages 319-330, 2018, doi: 10.1016/j.rser.2018.05.004.
[19] American Society of Civil Engineers, *Minimum design loads for buildings and other structures*. Reston, VA: American Society of Civil Engineers/Structural Engineering Institute, 2005. doi: 10.1061/9780784408094.
[20] A. Aghayere, and J. Vigil, "Structural wood design: ASD/LRFD". Boca Raton,Fl, USA: CRC Press; 2017.
[21] International conference of building officials, *Uniform building code, vol. 1, 1997 ed. Whittier, CA, USA: ICBO, 1997. [Online]. Available: https://www.scribd.com/document/74764949/UBC-Volume-1-1997. [Accessed: 22-Nov-2025].
[22] American Society of Civil Engineers, *Minimum design loads and associated criteria for buildings and other structures*, 7th ed. Reston, VA, USA: American Society of Civil Engineers (ASCE), 2017. doi: 10.1061/9780784414248.
[23] "Eurocode 3: Design of steel structures, EN 1993-1-1, European committee for standardization (CEN), Brussels, Belgium, 2005. [Online]. Available: https://gaprojekt.com/wp-content/uploads/2021/11/Eurocode-3-Design-Of-Steel-Structures.pdf. [Accessed: 22-Nov-2025].
[24] L. Hotma *et al.*, "Mesh convergence test by using finite element analysis (FEA) in shaft loading of 2kw induction motor," *Jurnal Rekayasa Mesin*, vol. 15, no. 3, pp. 1271–1280, Dec. 2024, doi: 10.21776/jrm.v15i3.1516.
[25] N. S. Gukop, P. M. Kamtu, B. D. Lengs, A. Babawuya, and A. Adegoke, "Effect of mesh density on finite element analysis simulation of a support bracket," *FUOYE Journal of Engineering and Technology*, vol. 6, no. 3, Sep. 2021, doi: 10.46792/fuoyejet.v6i3.632.
[26] C. Pisarciuc, I. Dan, and R. Cioară, "The influence of mesh density on the results obtained by finite element analysis of complex bodies," *Materials*, vol. 16, no. 7, p. 2555, Mar. 2023, doi: 10.3390/ma16072555.